

Employing semi-supervised learning for high-resolution segmentation of crystal defects

Ashish Chauniyal^{1*} | Pascal Thome^{2†} | Markus Stricker^{1*}

¹Interdisciplinary Centre for Advanced Materials Simulation (ICAMS), Ruhr-Universität Bochum, Univeristätstraße 150, 44780 Bochum, Germany

²Institute for Materials (IFM), Ruhr-Universität Bochum, Univeristätstraße 150, 44780 Bochum, Germany

Correspondence

Ashish Chauniyal, Interdisciplinary Centre for Advanced Materials Simulation (ICAMS) Ruhr-Universität Bochum, Univeristätstraße 150, 44780 Bochum, Germany
Email: ashish.chauniyal@rub.de

Funding information

NA

Materials characterization using electron backscatter diffraction (EBSD) requires indexing the orientation of the measured region from Kikuchi patterns. In the presence of defects the quality of the Kikuchi patterns can degrade. Or if the measured region contains a grain boundary, two or more orientations can cause pattern overlap which may lead to erroneous orientation calculations. In this work we show that constrained non-negative matrix factorization can be successfully employed to characterize such measurements containing signals from multiple crystallographic orientations, particularly if the misorientation is very small ($< 1^\circ$). Using simulated patterns, we demonstrate the resolution limit of the method and subsequently showcase a computationally efficient segmentation of a dendritic microstructure, which is on par with high resolution EBSD. By analysis of the weight metrics of the components across a grain boundary or dendrites, we demonstrate how very small misorientations/low-angle grain boundaries can be resolved at a pixel level. Our approach constitutes a versatile and robust tool complementing other fast indexing methods for microstructure characterization.

KEYWORDS

Kikuchi patterns, segmentation, semi-supervised learning, pattern overlap, grain boundary, HR-EBSD, RVB-EBSD

1 | INTRODUCTION

Electron backscatter diffraction (EBSD) has been the prime workhorse for the analysis of crystal structures and orientation of crystalline materials for many years (Engler and Randle, 2010; Graef et al., 2008). While the fundamental principles of diffraction and recording of Kikuchi patterns have not changed over the years, there has been continuous developments in novel ways of post-processing (Nolze et al., 2017). Starting from Hough-based indexing (Dingley and Randle, 1992; Adams et al., 1993; Wright and Adams, 1992; Lassen et al., 1992), which transforms the patterns to a Hough space followed by indexation, to the more recent Dictionary Indexing (DI) (Chen et al., 2015; Tanaka and Wilkinson, 2019; Lenthe et al., 2019) and pattern matching (Nolze et al., 2018, 2016) approaches, which directly compare the patterns to a simulated library and find out the best match. Such indexing methods process noisy patterns effectively and also provide good lateral and angular resolutions. The angular resolutions of EBSD has further been improved using cross-correlation methods that measure pattern shifts, along with the ability to quantify strains (Wright et al., 2011; Wilkinson, 2001; Wilkinson et al., 2006; Britton and Hickey, 2018; Thome et al., 2019; Wilkinson and Randman, 2010; Tanaka and Wilkinson, 2019). The cross-correlation-based methods thus provide a high resolution of angular variations by directly identifying sub-pixel level pattern shifts and go by the acronym high-resolution electron backscattered diffraction (HR-EBSD). Onwards from here with the progress of machine learning in material science, several data-based supervised machine learning (ML) methods have recently been employed for indexation and segmentation of microstructures (Jha et al., 2018; Shen et al., 2019; Kaufmann et al., 2020b,a; Ding et al., 2020; Lu et al., 2022). These methods circumvent the need to evaluate computationally expensive pattern comparisons and instead train a ML model that is adapted to the intricacies of the orientation space. While for routine tasks such methods are well suited, their robustness remains in question, as machine conditions, sample preparations, crystallography, and the need for large training datasets can greatly limit the extent to which such methods can be quickly deployed. An additional aspect is their transferability to *unseen* data. Due to the above reasons, it is generally desirable to employ unsupervised ML methods.

Unsupervised methods promise a higher efficiency and robustness (McAuliffe et al., 2020a). Several such unsupervised data-based approaches have been presented (McAuliffe et al., 2020a; Brewer et al., 2008; Wilkinson et al., 2019) which can discriminate between similar or dissimilar phases and improve the effective spatial resolution of automated EBSD analysis, particularly segmentation tasks. Denoising of electron backscattered diffraction patterns (EBSPs) is possible using (unsupervised) dimensionality reduction strategies (Ånes et al., 2020). For unsupervised methods an essential precept is that EBSPs are not directly mapped to orientations or phases in the standard EBSD sense, but instead undergo dimensionality reduction on raw pattern data followed by clustering (Wilkinson et al., 2019; McAuliffe et al., 2020a; Brewer et al., 2008). Herein, EBSP patterns are treated as linear combinations of spatially simple components (Brewer et al., 2008) which can then be used efficiently for segmentation. While the above methods do not directly provide the orientation information of the microstructure, they are still very useful in conjunction with standard EBSD methods. The most important advantage in this respect lies in the ability to segment and categorise data without prior knowledge of the crystallography of the microstructure. This implies that such methods are easily transferable to different types of microstructures without the need for expensive supervised training, often involving human-created masks or labels because these methods detect pattern existing in data without human bias.

The simplest dimensionality reduction algorithms that are used for EBSD data analysis, are principle component analysis (PCA) (Brewer et al., 2008; Wilkinson et al., 2019; Ånes et al., 2020) and non-negative matrix factorization (NMF) (McAuliffe et al., 2020a). NMF is shown to perform especially well for the segmentation of crystallographically similar phases, which extols the sensitivity of the technique in detecting very small changes in an EBSPs (McAuliffe et al., 2020a). So far, only a canonical NMF method has been implemented for segmentation which is essentially

a subset of PCA. However, the completely unsupervised nature of NMF implies that the derived NMF coefficients may not be amenable to physical interpretation. The derived NMF coefficients look similar to an EBSP with only small variations in intensities (McAuliffe et al., 2020a), however from an EBSD standpoint they cannot be directly associated with an orientation or a phase. For a connection to physics, the coefficients in such a factorization should be related to either an orientation or a phase, as well, which is not possible with canonical NMF. For this reason we need a factorization scheme that can exploit the prior knowledge of orientation or phases. Such a specialized factorization method is called constrained non-negative matrix factorization (cNMF) which incorporates the prior knowledge of one or all components during the factorization (Maffettone et al., 2021). In the context of EBSD, this translates to having a prior knowledge of certain EBSPs belonging to a particular orientation or phase. These known EBSPs need to be supplied externally during factorization and therefore the scheme can be classified as semi-supervised. In this work we implement a cNMF algorithm to factorize EBSPs using known EBSPs and calculate the weights of the components. These weights thus provide a metric to estimate the fraction of known EBSPs in any pattern. We show how this approach can be used to segment microstructures in great detail, which is on par with HR-EBSD (Thome et al., 2019) methods, with much less computational overhead.

Fixing components before factorization implies that we select certain EBSPs from the microstructure and then resolve the rest in terms of their weights with respect to these EBSPs. This approach of using *weight-based* metric to resolve a microstructure, subsequently allows us to address the problem of pattern overlaps at grain boundaries or other defects (Wright et al., 2014). The subject of pattern overlaps has been explored extensively in the past (Bate et al., 2005; Zaefferer, 2007; Wright et al., 2014; Tong et al., 2015; Singh et al., 2018; Tripathi and Zaefferer, 2019; Lenthe et al., 2020; Shi et al., 2021; Brodu et al., 2022; Fullwood et al., 2022) as it is well known that EBSD measurements nearby grain boundaries can create uncertainties in indexation. Inherent to EBSD measurements is the fact that the intensity contribution to the final pattern from each grain, when measured at a grain boundary, is related to the respective interaction volume of each grain. So far, the pattern overlap problem has been treated using rigorous pattern matching approaches which incorporate multiple crystal orientations (Shi et al., 2021; Tong et al., 2015; Lenthe et al., 2020), or by determining a resolution limit to avoid overlaps in the first place (Bate et al., 2005; Zaefferer, 2007; Fullwood et al., 2022). Yet, these approaches rely on mapping EBSPs to orientations. Even if these approaches lead to increase in accuracy, the volume fraction contribution from each grain may still remain unknown. Though the consideration of volume fraction has recently been made by simulating the mixing of Kikuchi patterns and subsequently matching patterns (Lenthe et al., 2020). Still, there is a need for employing a much less computationally expensive and more robust scheme.

In this regard, the work of Brewer et al. (2008) is most relevant to our work, as it employs a very simple yet robust PCA method to segment grains. Not only does this method deliver angular resolutions on par with standard EBSD, but can also discriminate between crystallographically similar phases. Furthermore, the authors foresaw the ability of PCA in deconvolving pattern overlaps, which can exceed the capabilities of EBSD. At the core of such analysis is the shift to a paradigm that EBSPs can be analyzed using an alternate metric, instead of orientations alone. In this work we follow this new paradigm of using alternate weight-based metric to characterize a microstructure (Brewer et al., 2008; Wilkinson et al., 2019; McAuliffe et al., 2020a). We employ an advanced data-based method - cNMF, which allows us to estimate the contribution of individual EBSPs in an overlapped EBSP using the weight metric. In this paper we briefly describe the cNMF method and explain its implementation for EBSPs. Thereafter, we first test the limits of the method on simulated patterns. We then present results pertaining to an experimental data set of low angle grain boundaries to showcase the segmentation ability for a limiting case of very small misorientations. This data set is specially chosen as it is synonymous to crystallographically similar EBSPs. Finally, we elaborate how to extract more information from the predicted values and discuss the identification of grain boundaries.

2 | METHODS

2.1 | Experimental Details

The specimen used for investigation is a cross-section of a cylindrical bar of single-crystalline superalloy ERBO1/C which is directionally solidified using a seeded Bridgeman technique (Hallensleben et al., 2017). This casting technique results in a single crystal along $\langle 001 \rangle$ direction. However, during solidification individual dendrites frequently deviate by small misorientation angles, which leads to a fine substructure (Thome et al., 2019). Cross-sections are carefully polished using a sequence of $6\mu\text{m}$, $3\mu\text{m}$ and $1\mu\text{m}$ diamond suspensions, followed by a 3 h Vibrometer polishing with a colloidal silica suspension of $0.25\mu\text{m}$ size. Finally, the surface has been cleaned by ion milling with 6 kV beam for 30 min at 40° inclination. The above steps are essential to obtain good quality Kikuchi patterns.

EBSD measurements are performed using a FEI Quanta 650 FEG SEM at 30 kV accelerating voltage, $60\mu\text{m}$ aperture, 17 mm working distance WD and 200 mm camera length (distance between detector and sample). Patterns are recorded using an EDAX-TSL system with a Hikari-XP camera at a resolution of 512×512 pixels, with a step size of $1\mu\text{m}$.

2.2 | Constrained Non-Negative Matrix Factorization

Constrained non-negative matrix factorization (cNMF) (Maffettone et al., 2021) is essentially a version of the canonical non-negative matrix factorization (NMF) where the former is semi-supervised and the latter is unsupervised. Starting with NMF first, for a given non-negative matrix \mathbf{X} of dimensions $m \times n$ we seek a factorization such that

$$\mathbf{X} \approx \mathbf{WH}, \quad (1)$$

where \mathbf{W} and \mathbf{H} are non-negative matrices of dimensions $m \times k$ and $k \times n$ respectively. Here k is the number of components which are provided by the user. The above then reduces to a minimization problem which can be solved as

$$\min_{\mathbf{W} \in \mathbb{R}^{m \times k}, \mathbf{H} \in \mathbb{R}^{k \times n}} D(\mathbf{X}, \mathbf{WH}), \quad (2)$$

such that $\mathbf{W} \geq 0$, $\mathbf{H} \geq 0$ and D is a separable, positive measure of fit. In the above, the β -divergence loss function is used for minimization (Févotte and Idier, 2011). β is the single shape parameter used in the minimization and we employ $\beta = 2$ or squared Euclidean distance given by

$$D_2(\mathbf{X}, \mathbf{X}') = \frac{1}{2} \sum_{i=1}^m \sum_{j=1}^n (\mathbf{X}_{i,j} - \mathbf{X}'_{i,j})^2 \quad (3)$$

An alternating non-negative least squares (ANLS) algorithm is used for minimization that operates by alternately minimizing $D_\beta(\mathbf{X}, \mathbf{WH})$ with respect to \mathbf{W} and \mathbf{H} such that all matrices are constrained to be non-negative. The above algorithm has been implemented with PyTorch by Maffettone et. al. (Maffettone et al., 2021) which is different from a canonically implemented NMF (McAuliffe et al., 2020a).

It is noted that the canonical NMF has some drawbacks (Maffettone et al., 2021) and from the standpoint of scientific data analysis, a major one is that the output components may not correspond to physically-interpretable entities. The above drawback is circumvented by using cNMF where the initial values for \mathbf{W} , \mathbf{H} - \mathbf{W}_0 and \mathbf{H}_0 respec-

tively, are constrained using prior knowledge and preset before the minimization as a constraint. Therefore, either the weights W_0 or components H_0 can be constrained at a time for factorization. In the following work, we constrain the components H_0 and solve for the corresponding weights. In the next section we describe how this mathematical framework is implemented for EBSP data.

2.3 | Data Processing

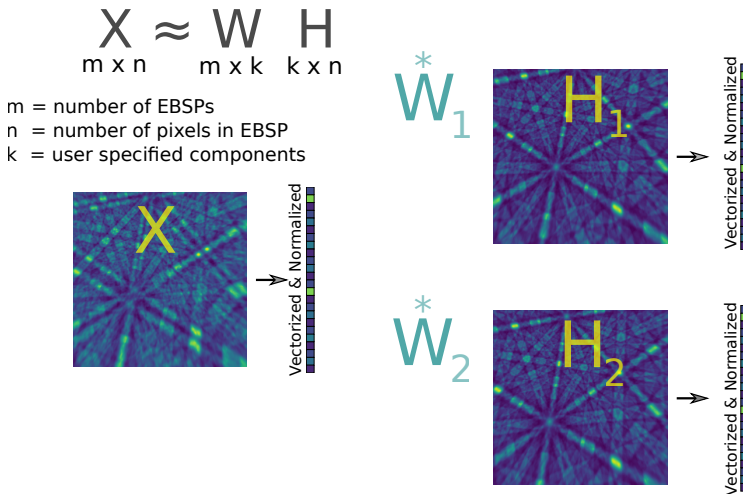


FIGURE 1 Schematic of the matrix algebra used in constrained non-negative matrix factorization. The data matrix X , the constrained components H (preset EBSPs) and the unknown weights W .

Each raw EBSP is first subtracted by a static background and a dynamic background but not processed further. Subsequently, the intensities for each pattern are normalized in the range 0 to 1 and vectorized as a single continuous vector. For the analysis of experimental data, the chosen region of interest is shown in Figure 3. Component EBSPs are selected from grain interiors marked by red markers in Figure 3. To obtain sharp component EBSPs from the marked regions, a 3x3 pixel area is selected and averaged using a Gaussian 3x3 kernel. These component patterns C_{1-6} are also shown in Figure 3.

The component patterns C_{1-6} shown in Figure 3 are very close w.r.t. their orientation. This can be rationalized based on the fact that the chosen microstructure is essentially a single crystal with only small amounts of misorientations ($< 0.1^\circ$), hence the patterns C_{1-6} *must* look very similar. Conventional Hough-based EBSD methods are unsuitable to analyze such a microstructure and, therefore, we employ the Rotation Vector Base Line (RVB)-EBSD method (Thome et al., 2019) for a baseline orientation mapping as reference. The RVB-EBSD method is an HR-EBSD technique specifically designed to study crystal mosaicity and fine microstructural details. Such microstructures are associated with slightly deviating growth paths of dendrites during directional solidification of Ni-based SX superalloys in a Bridgman process (Hallensleben et al., 2017). RVB-EBSD utilizes a normalized cross-correlation function along with a rotational vector baseline function to determine pattern shifts caused by changes in orientation relative to a selected reference pattern. This allows to detect small angular deviations ($< 0.1^\circ$) clearly. Therefore, consistently in this paper, we use the RVB-EBSD analyzed microstructure as a reference benchmark to compare our results obtained

using cNMF. For example in Figure 3, the central figure (orientation map) and Figure 5 (Kernel Average Misorientation). Additional details of the RVB-EBSD method and the applied color coding schemes can be found in the relevant publication (Thome et al., 2019).

To prepare data for cNMF, we first take note that each EBSD with a resolution of $n_{px} \times n_{px}$, is an image with gray values from 0-255 and therefore by construction non-negative. As described in Equation 1, \mathbf{X} forms a matrix with dimensions $m \times n$, where m is the number of independent measurements or scanned points and n is the feature dimension of an EBSD or total pixels $N = n_{px} \times n_{px}$. To analyze a grain boundary region between two grains, cNMF is carried out using only 2 known component patterns - $\mathbf{H}_1, \mathbf{H}_2$. These component patterns are selected from the C_{1-6} shown in Figure 3, depending on the analyzed region of interest. The constrained factorization then returns a pair of weights - \mathbf{W} corresponding to each component $\mathbf{H}_1, \mathbf{H}_2$. These 1-dimensional weights are then reshaped into respective 2-dimensional spatial dimensions for visualization. In this way we obtain 2 weight maps - w_1, w_2 , corresponding to each constrained component.

3 | RESULTS & DISCUSSION

3.1 | Mixing Simulated Patterns

As a first step, we test the theoretical angular resolution limits of the method using artificially generated overlapping patterns through intensity mixing (Brewer et al., 2008) that can be interpreted as a simulation of the conditions near a grain boundary (Tong et al., 2015). An arbitrary orientation is chosen and a Kikuchi pattern is extracted from a gnomonic projected space of a dynamically simulated master pattern (Callahan and De Graef, 2013). Similarly, another pattern is extracted with a relative misorientation angle ω with respect to the first pattern. These two patterns are linearly mixed into 20 intensity fractions, which includes the two original *pure* patterns as the limiting cases. Further data processing is the same as described in Section 2.3. Note however, that in this case the predicted weights are 1-dimensional, which can be compared to a linear behavior for verification. Figure 3 shows the resulting weights of the factorization of patterns oriented along [111] direction and misoriented by ω . We consider 4 cases in which ω is gradually decreased as $\omega = 5^\circ, 2.3^\circ, 1^\circ, 0.5^\circ$. The displayed overlapping patterns in Figure 2 correspond to the 10th index where there the original patterns are mixed with equal weight intensities.

Figure 2 (a) shows a superimposed Kikuchi pattern with visible overlap of two patterns, a common case in grain boundary regions. The predicted weights w_1 and w_2 for different mixing ratios follow the grey lines or the linear interpolation in the same manner as they are mixed. Note that the pattern overlap is clearly discernible in the image, due to a relatively large misorientation angle $\omega = 5^\circ$. Besides the misorientation, the result also highlights that very small changes in pattern intensities or weights are captured using cNMF as 20 different weights, and therefore mixing ratios, are successfully resolved. This is akin to crossing over a grain boundary in 20 discrete steps. In addition, each data point is independently predicted in cNMF. In other words, each EBSD is individually factorized, without any influence of the outcome of other data points.

With a decrease of ω to 2.3° in Figure 2 (b), it becomes difficult to visibly discern the overlap of two patterns. Instead, only a blur is visible, e.g. in the bottom left corner. Nevertheless, cNMF successfully predicts the calculated weights as per the linear mixing.

Further decrease of ω to 1° , shown in Figure 2 (c), leads to some data points which begin to deviate from linearity. Even though there is hardly any visible overlapping signature in the Kikuchi pattern itself, the cNMF method performs well even in this case.

A misorientation of $\omega = 0.5^\circ$, as shown in Figure 2 (d) constitutes a case beyond the resolution limit for factoriza-

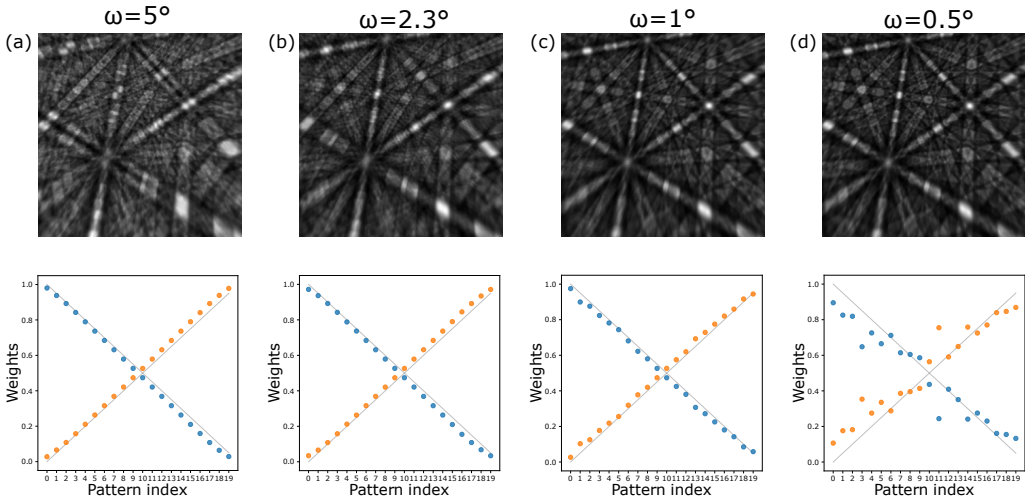


FIGURE 2 Constrained non-negative matrix factorization of a synthetic dataset showing predicted weights (points: blue = w_1 , orange = w_2), compared to linear behavior (grey lines). The misorientation angle between the component pattern used for synthetic EBSD generation is (a) $\omega = 5^\circ$ (b) $\omega = 2.3^\circ$ (c) $\omega = 1^\circ$ (d) $\omega = 0.5^\circ$. The Kikuchi patterns in each subfigure show the 10th pattern in the index that has equal ratio of mixing intensities.

tion. At this low misorientation angle, the weights cannot be determined accurately any more. However, such a small misorientation is not necessarily the limit of the method itself, but only selectively applies to the above dataset of 20 patterns. To attest to this, notice that even though the predicted weights deviate from absolute linearity, they still follow the linear trend. This implies that if the instead of 20 a lower number of patterns are factorized, the method may well predict better results. This scenario is akin to decreasing the number of steps when moving across the grain boundary. However, in this work we are only introducing a new method, so we refrain from such an analysis, which will be a part of a separate, future study.

Using the above analysis we are able to simultaneously test two parameters. The first is the sensitivity of cNMF to misorientation and the second is sensitivity to mixing steps. In practice the first is akin to resolving small misorientations between grains while the second is related to step size. We demonstrate that the cNMF method successfully predicts these variations. Moreover, we conclude that it is possible to locate grain boundaries in a microstructure using a weight based metric.

3.2 | Experimental Patterns

The use of simulated patterns is an essential step to test the limits the method but it is difficult to simulate real patterns containing noise, background signal, beamshifts, etc., and which are affected by sample surface quality, sample preparation artifacts, plastic deformation zones, surface relief and contamination issues. Therefore, in this section we apply cNMF on an experimental dataset of an ERBO1/C Ni-based single crystal superalloy specimen. The details of specimen preparation are provided in 2.1. This dataset is specifically selected due to the prevalence of low angle grain boundaries (the grains are within 1.5° orientation spread). This approach further tests the practical limits of the cNMF method by resolving patterns that are very similar (also see C_{1-6} in Figure 3). We compare our results to a RVB-EBSD based high-resolution analysis (Thome et al., 2019), which is state-of-the-art in analyzing such microstructures.

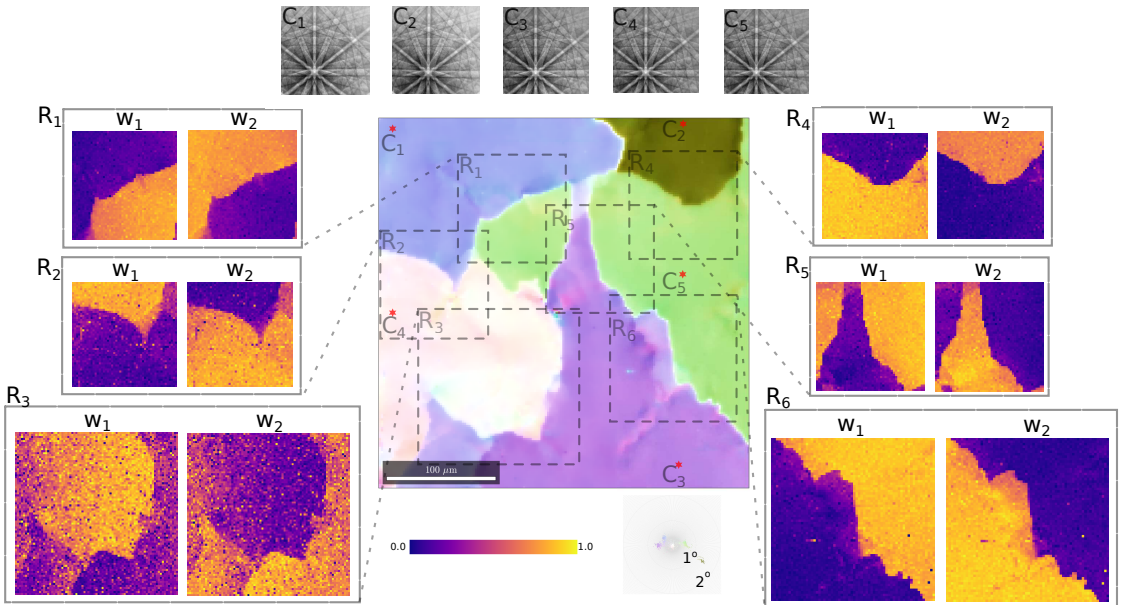


FIGURE 3 Weight maps of cNMF factorization chosen from different regions of the scanned area. The central figure shows the full scanned area and is colored according to a pole figure generated using RVB-EBSD method with the pole along a [001] direction as a 2° pole. Within the pole figure, specific regions are highlighted using red stars. They mark the locations chosen for the constrained components. Note that there are 5 locations of component patterns in total corresponding to 5 separate dendritic regions. All weight maps show a low-angle grain boundary between two regions and, correspondingly, two weight maps which show individual variations in weight w_1 and w_2 of the chosen patterns as constraints.

Figure 3 (R_{1-6}) shows the reconstructed weight maps using cNMF. The analysis is made using small sub-sections of the scanned area, such that each region of interest contains a low-angle grain boundary between two dendritic regions. The constrained components for each region are extracted from within the grain interior marked C_{1-6} with red stars. For example, in region R_1 the constrained component EBSPs are C_1 and C_5 . Similarly for region R_5 they are C_3 and C_5 . In this manner, corresponding to each component combination, a weight map is obtained, shown using w_1 and w_2 . Note that the weight maps are shown using both w_1 and w_2 as both together can be used as indicators to demonstrate variations in each individual weight. Unlike the synthetic pattern analysis consisting of superimposed patterns in section 3.1, in this case only the grain boundary EBSPs are expected to exhibit pattern overlaps whereas a single pattern (orientation) typically dominates in the grain interior. This can be seen in Figure 3 region R_1 , where each weight map w_1 , w_2 has distinct bright and dark colored regions which invert symmetrically across the grain boundary. That is, weights are inversely proportional which allows us to demarcate the extent of each grain. Notice that in terms of misorientation, each pair of two grains lie within 1° pole as shown in the RVB-EBSD pole figure in the center bottom. In addition, also note that in the pole figure the grain boundary pixels may not be indexed to distinct orientations because of pattern overlap (the grain boundary pixels are white), which is not the case with weight maps w_1 , w_2 . Thus, using weights, the extent of the grain boundary is distinctly known. Furthermore, in the weight map w_1 the intensity of the pixels varies within the grain which is indicative of small orientation changes, consistent with the RVB-EBSD pole figure.

In region R_4 , the grain boundary is clearly visible in the weight maps. Interdendritic orientations, however, are not visible, consistent with RVB-EBSD pole figure.

In region R_5 , two boundaries exist between intersecting dendritic regions which consist of only 2 grains. The corresponding weight maps exhibit similar pixel intensities that lie within the same grain which distinctly demarcates the grain boundaries. Moreover, weight map w_2 shows a variation in intensity within the respective grain (bottom left), that is consistent with interdendritic orientation changes in the pole figure.

In region R_6 , weight maps demarcate the extent of the grain boundary as well as local changes in orientation along the grain boundary in map w_2 . The above cases demonstrate that cNMF is able to detect orientation variations which are on par with the RVB-EBSD reference (orientations changes are less than 0.25°). Note however, the variations in intensities in region R_6 within a dendritic region implicitly arise due to sensitivity of the method as the factorized EBSPs are dissimilar to the component EBSPs. This implies that deviations from the component pattern lead to changes in weights, even though they arise from pattern degradation and not alone from orientation changes. Following this, it can also be argued that all EBSPs that deviate from the two chosen component EBSPs may correspond to a 3rd orientation or grain.

This aspect is brought out more clearly in region R_2 where, apart from a grain boundary, a triple junction exists in the top right corner. In the weight maps w_1 , w_2 , two dominant grains are distinctly visible. Herein, the constrained components are C_1 , C_4 . Yet, the predicted weights in the 3rd intersecting dendritic region (right corner), which is not used as component in cNMF, are very similar in intensities for both w_1 and w_2 maps. Thus, attesting to the argument that any orientation that is not used in cNMF may still manifest itself in the form of weight intensity variation. This, generally, allows the segmentation of more than two grains even if only two components are used, albeit with some loss of accuracy. More discussion on this aspect is provided within Section 3.4.

In Region R_3 , the component EBSPs are located at C_3 and C_4 , where there is a change in orientation within the left grain. In other words, the grain boundary region is slightly misoriented to the orientation of the C_4 location. Furthermore, the misorientation angle between the two grains is lowest in this region ($\approx 0.5^\circ$) as shown in the central pole figure. Consequently, the calculated weight maps exhibit a considerable amount of noise even through the demarcation of dendritic and interdendritic grain boundaries are successfully identified. Thus, this case forms the

limiting case of the cNMF method. Moreover, this demonstrates that the weight maps are sensitive to the location of the selected component patterns in the scan space with respect to the region of interest.

3.3 | Resolving the grain boundaries

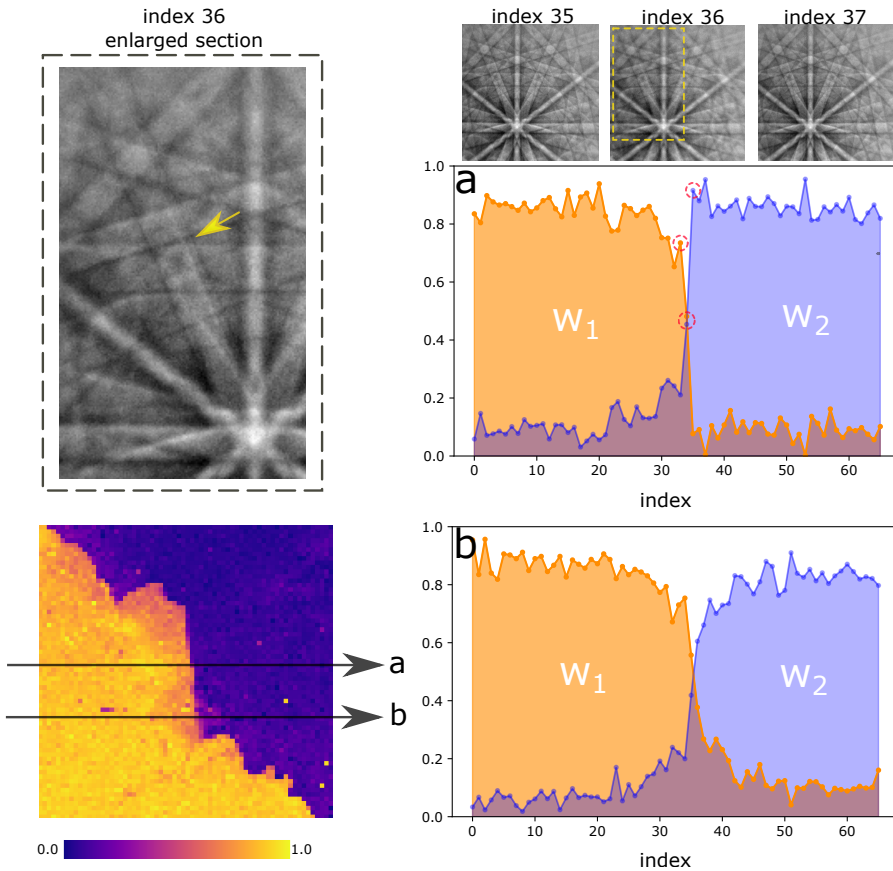


FIGURE 4 Profiles of individual weights w_1 , w_2 across two grain boundaries: (a) sharp boundary and (b) smeared boundary. The weight map w_1 of region R_6 is used to depict the microstructure. Along profile 'a', the EBSPs at 3 points at the grain boundary from index 35-37 are shown. The location of these EBSPs along the profile are indicated with red circles in (a). The enlarged section of the EBSP at index 36 is shown where a faint signature of pattern overlap is visible and indicated with a yellow arrow.

Using a weight based metric instead of orientation allows us to resolve grain boundaries by leveraging the change in weights and, thereby, address the issue of pattern overlaps. Consider Figure 4, which shows the weight profiles across a grain boundary for two cases - (a) across where orientation appears to transition sharply from one pixel to the other and (b) where the grain boundary appears *smeared* out. Along profile (a), weights w_1 and w_2 exhibit a discrete step-like change across the grain boundary. Notice the relative symmetric reversal of the weights across the grain boundary. This implies that the grain boundary is sharp and patterns do not have a measurable overlap within the

grain interior but only at the interface. To better explore this behavior we consider three distinct patterns which lie along the grain boundary profile (a). Pattern indices 35,36,37 lie across profile 'a' at the transition from left grain to the right. Their respective weights are marked with red circles in the Figure 4(a). Pattern 36 exhibits an overlap of patterns 35 and 37 which is, however, very hard to visually discern. An enlarged section of pattern 36 shows a faint secondary band marked by a yellow arrow. This indicates that there is some pattern overlap of patterns 35 and 37 which is successfully resolved. The above results thus depict a use case which is comparable to the scenario tested using simulated patterns in Section 3.1.

On the other hand, along profile 'b', weights w_1 and w_2 exhibit a gradual change across the grain boundary. Across the grain boundary along profile 'b', the weight map shows a visibly smeared grain boundary which indicates that the orientation changes gradually. Nevertheless, the position of the grain boundary can be estimated at the point where the two weights w_1 , w_2 make a transition. This scenario is comparable to the scenario where the grain boundary is crossed in several steps as discussed previously (Sec. 3.1). Herein, the relative transition of weights w_1 , w_2 can also be exploited to estimate the location of the grain boundary.

To locate the grain boundary, we need to extract the information contained implicitly in the weight metric. The transition between very similarly oriented regions can be captured by calculating the absolute differences in weights $abs|w_1 - w_2|$ per pixel since pixels at the grain boundary have similar or equal weights as a consequence of pattern mixing. Consequently, the absolute difference in weight is lower at and near grain boundary region compared to the grain interior (also consider the weight profile in Figure 4 for an intuition). To test this hypothesis, we show the absolute weight difference maps of separate regions in Figure 5. For comparison, we additionally present a Kernel Average Misorientation (KAM) map for the same region as obtained using RVB-EBSD (Thome et al., 2019).

In Figure 5, region R_1 , the grain boundary is revealed as dark colored pixels, where as the brighter pixels belong to the grain interior. This follows from the hypothesis that the absolute difference in weights in the darker pixels should be lowest while the grain interiors would show relatively larger values. A comparison with the KAM sub-region shows that in the difference weight map the grain boundary is much sharper and well defined. Other interesting features are the apparent discontinuities in dark pixels at the grain boundary which may be understood as a consequence of the step size and orientation of the grain boundary with respect to the scan direction (Tripathi and Zaefferer, 2019). Darker pixels are clustered around regions where the grain boundary curvature changes. Local orientation changes arising from sub-grain boundaries are also visible in these maps as variations in intensity. Overall, it is possible to resolve a grain boundary at the level of a pixel. This resolution would not be possible using a KAM analysis as each pixel is assigned to a particular orientation which then leads to an average misorientation with respect to the surrounding pixels. In other words, depending upon the size of the kernel, a grain boundary will always be a few pixels wide and also continuously connected.

Our proposed approach is capable of detecting regions of pattern overlaps very effectively and efficiently. In cases where minimal overlap exist, we can nevertheless capture the relative variations from one grain to the other. For example, in Figure 5, region R_5 , the grain boundary can be identified as different pixel intensities in the two grains. This allows us to sharply demarcate the grain boundary. A similar scenario unfolds in Figure 5, region R_4 , where the grain extent is distinctly demarcated as a change in mean intensity, along with some darker pixels at the grain boundary. That is, the left grain is brighter than the right grain and separated by a dark grain boundary region.

Even maps derived from noisy weight maps, such as Figure 5, region R_2 , allows the detection of the grain boundary region very accurately. Another interesting feature is notable in this region. The small portion of a third grain (top right) manifests in the form of dark pixels. Understandably so, because the absolute difference scheme entails low intensity pixels for that portion of the map, which belongs to a 3rd grain orientation which is not part of the constraints. This, in principle, allows to resolve triple junctions around this region similar to the predictions of Brewer (Brewer et al.,

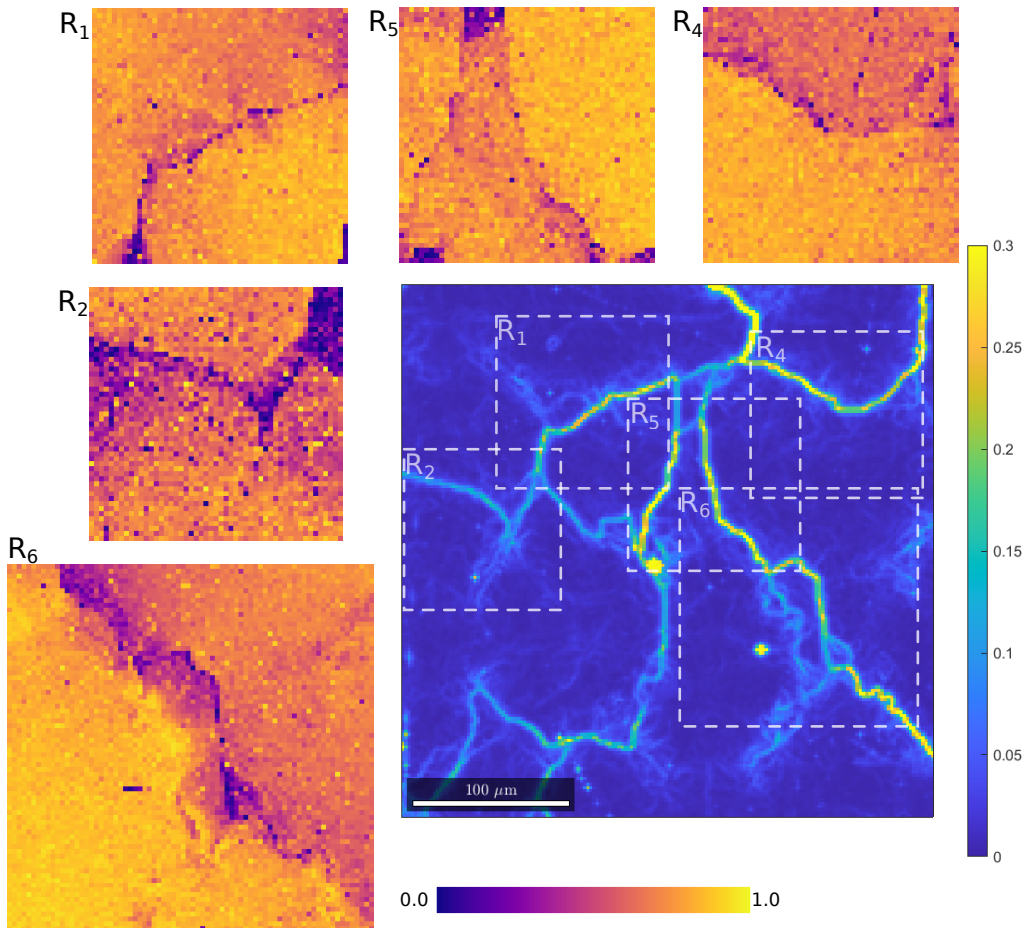


FIGURE 5 Absolute weight difference maps of different regions and comparison to a KAM map. The KAM map is obtained after processing the pole figure map in Figure 3. Enlarged versions of the regions are shown in their correct relative size. The highlighted regions are the same as selected in Figure 3.

2008). However, the analysis of triple junctions does not lie within the scope of the present work but can be subject of future studies.

Finally, Figure 5, region R_6 , reveals that a combination of the previously described scenarios can be present. The grain boundary is sharp and denoted by dark pixels in specific regions. A relative variation of mean intensity exists between the two adjoining grains, thereby allowing us to demarcate the extent of each grain. That is, the left grain is brighter than the right grain. In addition, some areas around the grain boundary show substantially darker and smeared-out transitions at the grain boundary. This can be rationalized as a combined effect of the presence of sub-grain structures and because the component EBSPs are slightly different from the sub-grain structure EBSPs. These features, however, only show up as gradual variations in intensity.

3.4 | General discussion

First and foremost, the cNMF method provides a novel method of segmentation as compared to an orientation indexing approach. The use of a weight metric to resolve the extent of each grain allows us to capture orientation changes within the grain as well, which is on par with HR-EBSD methods. While the weight maps shown in Figure 3 belong to a grain boundary between only two grains, it is in principle also possible to resolve larger areas. For example in Figure 6, a two-component segmentation with one weight map is enough to demarcate the extent of dendrites and interdendritic features. In the figure w_1 map shows the intensity of weights which are most similar to the component EBSP at C_3 . Notice the level of detail within the large dendrite that can be captured along with a clear demarcation of grain boundaries. To further extend the same idea, we can also calculate multiple two-component factorizations and then combine the results together. For example in Figure 7 four different instances of factorization are shown with component EBSPs originating from the grain interiors. These four weight-maps are then combined to form a 4 channel color composite image that shows the microstructure in fine detail. Herein, similarity in colors signify similarity of orientation as well.

Note that this is possible in our experimental data set because the patterns belong to similarly-oriented grains or very similar EBSPs. In case of large angle grain boundaries, the regions which deviate substantially from the grain of interest exhibiting low intensities. This may be construed as a drawback of the method. However, we propose our method as a companion tool useful in special cases such as those presented above or in segmentation problems where indexing crystallographically similar phases creates its own problems (McAuliffe et al., 2020a; Lenthe et al., 2020).

The second key aspect of using cNMF is the ability to factorize overlapping pattern into their constituents which follows a paradigm of employing a weight-based metric. This is advantageous as the binary classification of a pixel that is used in orientation imaging (Tong et al., 2015) is avoided. So far, the method of reducing the resolution of the scan step is used to accurately resolving grain boundaries (Zaefferer, 2007). However, a weight-driven approach can allow to clearly locate a grain boundary without changing the resolution limits (accelerating voltage) of the electron beam itself. A continuous variable in the form of weights allows us to appreciate the smooth transitions across a grain boundary and detect EBSPs with pattern overlaps distinctly. These transitions may arise either due to inherent orientation changes or due to the step size during measurement. Following the analysis in Sections 3.1 and 3.3, we can also argue that the grain boundary can be resolved to a single pixel, irrespective of the step size. That is, the most probable location of the grain boundary should be at pixels with largest amount of overlaps. This aspect of cNMF can be particularly useful in spatially resolving nanoscale phases where the electron-matter interaction volume is of comparable size to the characteristic length scale of the phase (Brodu et al., 2022). In which case resolving pattern overlaps and cleaning data is of utmost importance for proper characterization. Thus cNMF can prove to be a viable alternate.

Finally, a comment on the robustness and efficiency of cNMF. The method is already in use for various scientific analysis (Maffettone et al., 2021) and allows for enormous flexibility in the input data. We have implemented the scheme for EBSD data analysis using EBSPs. In practice, however, a variety of signals can be used, as the method is not affected by material/signal/dimensions and therefore can work for different crystallographic orientations and phases. For example, locating the boundaries of γ/γ' phases in superalloys (Gamanov et al., 2023). In addition, our proposed scheme would also work for a hybrid dataset where energy dispersive X-ray spectroscopy (EDS) data can be combined with EBSP signal (McAuliffe et al., 2020b), i.e. use a multimodal representation of a material or part of it. With respect to efficiency, since each pattern/signal can be read and factorized independently it is also possible to parallelize for GPUs. In terms of speed, the method is less computationally expensive than the HR-EBSD methods but like such methods, requires storing Kikuchi patterns. Some part of this storage space can be minimized by only analyzing small grain boundary regions on the fly and discarding after analysis. Furthermore, the pattern overlap detection of cNMF can still be used efficiently within the standard indexing procedure, as an add-on. To close, we note that any existing dataset where Kikuchi patterns are recorded can be re-analyzed, since our proposed method does not depend on any specific measurement settings or crystallographic information. Consequently more information regarding phases, orientations and defects can be extracted from already existing datasets.

4 | CONCLUSIONS

We implement a semi-supervised constrained non-negative factorization (cNMF) method to segment and demarcate grain boundaries. Using linear superpositions of synthetic patterns, we demonstrate the angular sensitivity and resolution of this technique. The process *simulates* two scenarios simultaneously - (1) the sensitivity to misorientation between patterns (2) sensitivity to mixing steps. Our method performs well in resolving misorientations considerably $< 1^\circ$. This proves that the method can work effectively, in particular for low-angle grain boundaries.

To test the limiting case of grain boundary segmentation (LAGB), we demonstrate the use of the method on a dataset of a technical single crystal superalloy. The specimen comprises of dendrites which deviate by small misorientation angles, $\omega < 1^\circ$. Using cNMF, the grain boundary regions are segmented using *weight maps*. Inherent to the method is the paradigm of segmenting a microstructure in the form of weights w.r.t. to user-defined references instead of absolute orientations. The weight maps clearly segment the grains and show features which are on par with RVB-EBSD method - an HR-EBSD technique specifically designed for mapping small misorientations during dendritic growth. Using the weight metric, we are able to consider overlaps in patterns and show how more information can be extracted from the data. The regions of highest pattern overlaps are regions where the absolute difference in weights is lowest. Using this metric, the grain boundary can be resolved even at a pixel level, albeit with some nuances, which are discussed in detail.

The cNMF method is versatile and may find use in applications such as grain and phase segmentation with similar EBSPs and small-scale phases with extensive overlapping EBSPs. Furthermore, due to its robustness, hybrid signals can be used which use a combination of both EBSP and EDS signals. While the processing speed may still be slower than the standard indexing speeds today, the method can be useful when used in conjunction with orientation imaging methods or in localized regions.

Appendix

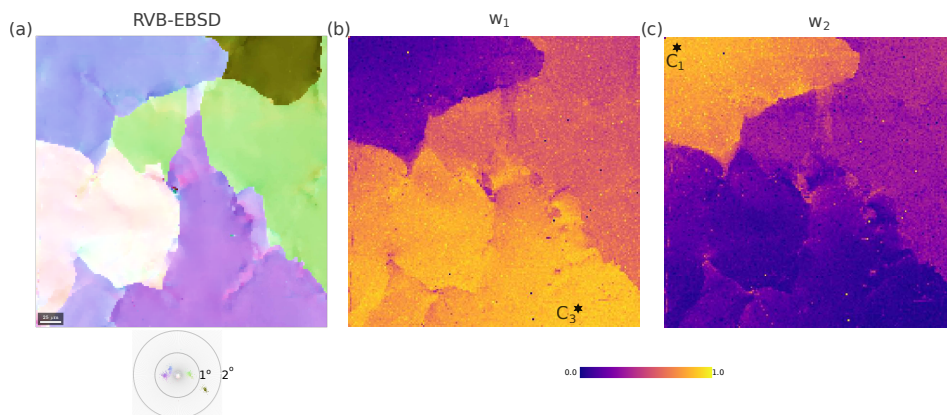


FIGURE 6 A1: cNMF factorization of the entire region of interest using weight-maps w_1 - (b) and w_2 - (c). The component EBSPs originate from C_1 and C_3 which have also been marked. For comparison an RVB-EBSD generated pole figure has also been provided - (a)

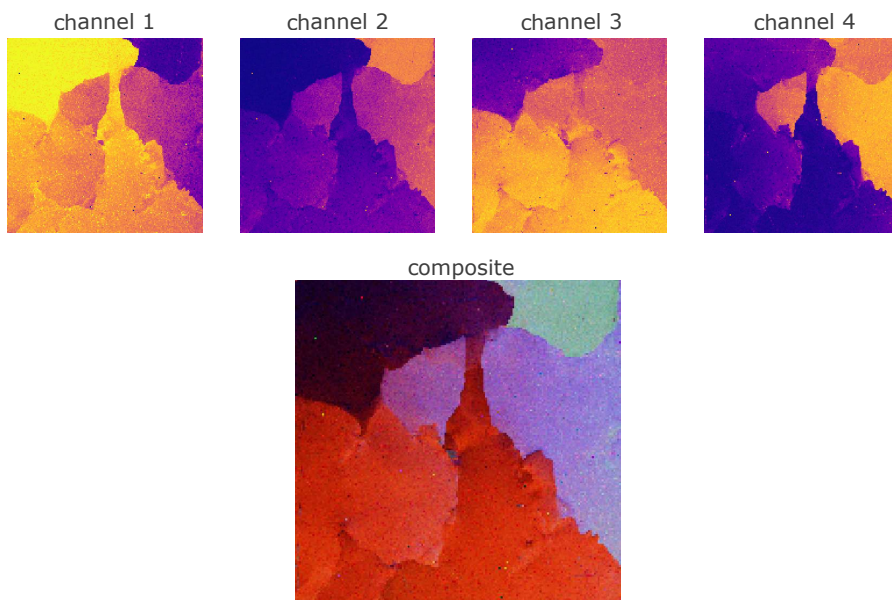


FIGURE 7 A2: Constitution of a 4 channel composite color image formed by combining 4 weight-maps of the entire region of interest.

references

- Adams, B. L., Wright, S. I. and Kunze, K. (1993) Orientation imaging: The emergence of a new microscopy. *Metallurgical Transactions A*, **24**, 819–831. URL: <https://doi.org/10.1007/BF02656503>.
- Ånes, H. W., Hjelen, J., Sorensen, B. E., Van Helvoort, A. T. and Marthinsen, K. (2020) Processing and indexing of electron backscatter patterns using open-source software. *IOP Conference Series: Materials Science and Engineering*, **891**.
- Bate, P. S., Knutsen, R. D., Brough, I. and Humphreys, F. J. (2005) The characterization of low-angle boundaries by EBSD. *Journal of Microscopy*, **220**, 36–46.
- Brewer, L. N., Kotula, P. G. and Michael, J. R. (2008) Multivariate statistical approach to electron backscattered diffraction. *Ultramicroscopy*, **108**, 567–578.
- Britton, T. B. and Hickey, J. L. (2018) Understanding deformation with high angular resolution electron backscatter diffraction (HR-EBSD). *IOP Conference Series: Materials Science and Engineering*, **304**.
- Brodu, E., Winkelmann, A. and Seefeldt, M. (2022) A Pattern Processing Method to Map Nanoscale Phases by EBSD. *Microscopy and Microanalysis*, **28**, 716–722.
- Callahan, P. G. and De Graef, M. (2013) Dynamical electron backscatter diffraction patterns. Part I: Pattern simulations. *Microscopy and Microanalysis*, **19**, 1255–1265.
- Chen, Y. H., Park, S. U., Wei, D., Newstadt, G., Jackson, M. A., Simmons, J. P., De Graef, M. and Hero, A. O. (2015) A Dictionary Approach to Electron Backscatter Diffraction Indexing. *Microscopy and Microanalysis*, **21**, 739–752.
- Ding, Z., Pascal, E. and De Graef, M. (2020) Indexing of electron back-scatter diffraction patterns using a convolutional neural network. *Acta Materialia*, **199**, 370–382. URL: <https://doi.org/10.1016/j.actamat.2020.08.046>.
- Dingley, D. J. and Randle, V. (1992) Microtexture determination by electron back-scatter diffraction. *Journal of Materials Science*, **27**, 4545–4566. URL: <https://doi.org/10.1007/BF01165988>.
- Engler and Randle, V. (2010) *Introduction to texture analysis: macrotexture, microtexture, and orientation mapping*. London: CRC Press London.
- Févotte, C. and Idier, J. (2011) Algorithms for Nonnegative Matrix Factorization with the β -Divergence. *Neural Computation*, **23**, 2421–2456.
- Fullwood, D. T., Sanderson, S., Baird, S., Christensen, J., Homer, E. R. and Johnson, O. K. (2022) Determining Grain Boundary Position and Geometry from EBSD Data: Limits of Accuracy. *Microscopy and Microanalysis*, **28**, 96–108.
- Gamanov, S., Dlouhy, A., Bürger, D., Eggeler, G. and Thome, P. (2023) Evolution of local misorientations in the γ/γ' -microstructure of single crystal superalloys during creep studied with the rotation vector baseline (RVB) EBSD method. *Microscopy Research and Technique*, 1–18.
- Graef, M., McHenry, M. and Keppens, V. (2008) Structure of Materials: An Introduction to Crystallography, Diffraction, and Symmetry. *The Journal of the Acoustical Society of America*, **124**, 1385.
- Hallensleben, P., Schaar, H., Thome, P., Jöns, N., Jafarizadeh, A., Steinbach, I., Eggeler, G. and Frenzel, J. (2017) On the evolution of cast microstructures during processing of single crystal Ni-base superalloys using a Bridgman seed technique. *Materials & Design*, **128**, 98–111. URL: <https://www.sciencedirect.com/science/article/pii/S0264127517304665>.
- Jha, D., Singh, S., Al-Bahrani, R., Liao, W. K., Choudhary, A., De Graef, M. and Agrawal, A. (2018) Extracting grain orientations from EBSD patterns of polycrystalline materials using convolutional neural networks. *Microscopy and Microanalysis*, **24**, 497–502.

- Kaufmann, K., Zhu, C., Rosengarten, A. S., Maryanovsky, D., Harrington, T. J., Marin, E. and Vecchio, K. S. (2020a) Diffraction Using Machine Learning. *Science*, **367**, 564–568.
- Kaufmann, K., Zhu, C., Rosengarten, A. S., Maryanovsky, D., Wang, H., Vecchio, K. S. and Vecchio, K. S. (2020b) Phase Mapping in EBSD Using Convolutional Neural Networks. *Microscopy and Microanalysis*, **26**, 458–468.
- Lassen, N. C., Jensen, D. J. and Conradsen, K. (1992) Image processing procedures for analysis of electron back scattering patterns. *Scanning Microscopy*, **6**, 115–121.
- Lenthe, W. C., Germain, L., Chini, M. R., Gey, N. and De Graef, M. (2020) Spherical indexing of overlap EBSD patterns for orientation-related phases – Application to titanium. *Acta Materialia*, **188**, 579–590. URL: <https://doi.org/10.1016/j.actamat.2020.02.025>.
- Lenthe, W. C., Singh, S. and Graef, M. D. (2019) A spherical harmonic transform approach to the indexing of electron back-scattered diffraction patterns. *Ultramicroscopy*, **207**, 112841. URL: <https://doi.org/10.1016/j.ultramicro.2019.112841>.
- Lu, Q., Wu, J., Liu, S., Zhang, S., Cai, X., Li, W., Jiang, J. and Jin, X. (2022) Revealing geometrically necessary dislocation density from electron backscatter patterns via multi-modal deep learning. *Ultramicroscopy*, **237**.
- Maffettone, P. M., Daly, A. C. and Olds, D. (2021) Constrained non-negative matrix factorization enabling real-time insights of in situ and high-throughput experiments. *Applied Physics Reviews*, **8**.
- McAuliffe, T. P., Dye, D. and Britton, T. B. (2020a) Spherical-angular dark field imaging and sensitive microstructural phase clustering with unsupervised machine learning. *Ultramicroscopy*, **219**, 113132. URL: <https://doi.org/10.1016/j.ultramicro.2020.113132>.
- McAuliffe, T. P., Foden, A., Bilsland, C., Daskalaki Moutanou, D., Dye, D. and Britton, T. B. (2020b) Advancing characterisation with statistics from correlative electron diffraction and X-ray spectroscopy, in the scanning electron microscope. *Ultramicroscopy*, **211**, 112944. URL: <https://doi.org/10.1016/j.ultramicro.2020.112944>.
- Nolze, G., Hielscher, R. and Winkelmann, A. (2017) Electron backscatter diffraction beyond the mainstream. *Crystal Research and Technology*, **52**, 1–24.
- Nolze, G., Jürgens, M., Olbricht, J. and Winkelmann, A. (2018) Improving the precision of orientation measurements from technical materials via EBSD pattern matching. *Acta Materialia*, **159**, 408–415.
- Nolze, G., Winkelmann, A. and Boyle, A. P. (2016) Pattern matching approach to pseudosymmetry problems in electron backscatter diffraction. *Ultramicroscopy*, **160**, 146–154. URL: <http://dx.doi.org/10.1016/j.ultramicro.2015.10.010>.
- Shen, Y. F., Pokharel, R., Nizolek, T. J., Kumar, A. and Lookman, T. (2019) Convolutional neural network-based method for real-time orientation indexing of measured electron backscatter diffraction patterns. *Acta Materialia*, **170**, 118–131.
- Shi, Q., Zhou, Y., Zhong, H., Loinsard, D., Dan, C., Zhang, F., Chen, Z., Wang, H. and Roux, S. (2021) Indexation of electron diffraction patterns at grain boundaries. *Materials Characterization*, **182**.
- Singh, S., Guo, Y., Winiarski, B., Burnett, T. L., Withers, P. J. and De Graef, M. (2018) High resolution low kV EBSD of heavily deformed and nanocrystalline Aluminium by dictionary-based indexing. *Scientific Reports*, **8**, 1–8.
- Tanaka, T. and Wilkinson, A. J. (2019) Pattern matching analysis of electron backscatter diffraction patterns for pattern centre, crystal orientation and absolute elastic strain determination – accuracy and precision assessment. *Ultramicroscopy*, **202**, 87–99. URL: <https://doi.org/10.1016/j.ultramicro.2019.04.006>.
- Thome, P., Medghalchi, S., Frenzel, J., Schreuer, J. and Eggeler, G. (2019) Ni-base superalloy single crystal (SX) mosaicity characterized by the Rotation Vector Base Line Electron Back Scatter Diffraction (RVB-EBSD) method. *Ultramicroscopy*, **206**, 112817. URL: <https://doi.org/10.1016/j.ultramicro.2019.112817>.

- Tong, V., Jiang, J., Wilkinson, A. J. and Britton, T. B. (2015) The effect of pattern overlap on the accuracy of high resolution electron backscatter diffraction measurements. *Ultramicroscopy*, **155**, 62–73. URL: <http://dx.doi.org/10.1016/j.ultramic.2015.04.019>.
- Tripathi, A. and Zaefferer, S. (2019) On the resolution of EBSD across atomic density and accelerating voltage with a particular focus on the light metal magnesium. *Ultramicroscopy*, **207**, 112828. URL: <https://doi.org/10.1016/j.ultramic.2019.112828>.
- Wilkinson, A. J. (2001) A new method for determining small misorientations from electron back scatter diffraction patterns. *Scripta Materialia*, **44**, 2379–2385.
- Wilkinson, A. J., Collins, D. M., Zayachuk, Y., Korla, R. and Vilalta-Clemente, A. (2019) Applications of multivariate statistical methods and simulation libraries to analysis of electron backscatter diffraction and transmission Kikuchi diffraction datasets. *Ultramicroscopy*, **196**, 88–98. URL: <https://doi.org/10.1016/j.ultramic.2018.09.011>.
- Wilkinson, A. J., Meaden, G. and Dingley, D. J. (2006) High-resolution elastic strain measurement from electron backscatter diffraction patterns: New levels of sensitivity. *Ultramicroscopy*, **106**, 307–313.
- Wilkinson, A. J. and Randman, D. (2010) Determination of elastic strain fields and geometrically necessary dislocation distributions near nanoindenters using electron back scatter diffraction. *Philosophical Magazine*, **90**, 1159–1177.
- Wright, S. I. and Adams, B. L. (1992) Automatic analysis of electron backscatter diffraction patterns. *Metallurgical Transactions A*, **23**, 759–767.
- Wright, S. I., Nowell, M. M., De Kloe, R. and Chan, L. (2014) Orientation precision of electron backscatter diffraction measurements near grain boundaries. *Microscopy and Microanalysis*, **20**, 852–863.
- Wright, S. I., Nowell, M. M. and Field, D. P. (2011) A review of strain analysis using electron backscatter diffraction. *Microscopy and Microanalysis*, **17**, 316–329.
- Zaefferer, S. (2007) On the formation mechanisms, spatial resolution and intensity of backscatter Kikuchi patterns. *Ultramicroscopy*, **107**, 254–266.

Data statement

The Kikuchi pattern data set can be downloaded from Zenodo (<https://doi.org/10.5281/zenodo.10705510>). An up-to-date version of the implementation of cNMF is available from a github repository (https://gitlab.ruhr-uni-bochum.de/icams-mids/kikuchi_cnmf.git).

Conflict of interests

The authors declare no competing financial interests or personal relationships that could have influenced this work.